On the influence of the adhesive and the adherend ductility on mode I fracture characterization of thick adhesively-bonded joints

Saleh, Mohamed Nasr; Budzik, Michal K.; Saeedifar, Milad; Zarouchas, Dimitrios; Teixeira De Freitas, Sofia

On the influence of the adhesive and the adherend ductility on mode I fracture characterization of thick adhesively-bonded joints

Mohamed Nasr Saleh [a,b,*], Michal K. Budzik [c], Milad Saeedifar [a], Dimitrios Zarouchas [a], Sofia Teixeira De Freitas [a]

[a] *Structural Integrity & Composites, Faculty of Aerospace Engineering, Delft University of Technology, Delft, 2629 HS, the Netherlands*
[b] *Advanced Materials Research Center, Technology Innovation Institute, Masdar City, Abu Dhabi, United Arab Emirates*
[c] *Department of Mechanical and Production Engineering, Aarhus University, Inge Lehmanns Gade 10, Aarhus, 8000, Denmark*

ARTICLE INFO

ABSTRACT

Thicker bondlines along with manufacturing-tolerant and fracture-resistant adhesives are trends visible across different industries, especially maritime. In this work, two contrasting adhesives: an elastic-brittle epoxy-based, and a nonlinear-ductile methyl methacrylate (MMA) are characterized and compared via tensile, compact tension (CT) and double cantilever beam (DCB) testing, for steel-to-steel adherends. Significant differences are captured between the two bonding materials in terms of the energy required for crack growth: in the MMA "ductile" adhesive is ~4 and 10 times more than for the epoxy "relatively brittle" adhesive for CT and DCB testing, respectively. While epoxy bondlines fail due to a symmetric in-plane crack, the MMA bondlines experience multiple cracking originating from high deformations and Poisson's effects. Moreover, in the case of MMA adhesive, the DCB testing led to plastic deformation of steel adherends. The existing evaluation protocols are adopted for data reduction and the effect of plastic dissipation is theoretically addressed. Despite adherend plasticity, it is concluded that the crack growth is driven by the elastic energy release, and thus, after small correction taking into account initial adherend plasticity, the existing simple models can still be used. This study highlights the potential use of ductile adhesive instead of the commonly used brittle ones to significantly improve the adhesively bonded joints in maritime applications in which thick bondlines, manufacturing-tolerant and fracture-resistance characteristics are required.

1. Introduction

The potential of using composite materials in e.g. maritime applications and structures has drawn more interest and attention in the past decades [1]. Using composite materials in maritime structures can offer several advantages such as: weight savings, lower CO_2 emissions, energy savings and corrosion resistance [2]. This consequently can lead to increased payload capacity for ships as well as lower transportation costs. In spite of all the advantages that composite structures incorporation can offer, there are some challenges facing their widespread. One major challenge is joining and assembly of composite structures to the traditional metal structures, such as the ship steel hull. Historically, in the maritime industry, joining has been always done using welding. However, with the introduction of light-weight composite structures to achieve weight and cost reductions, alternative joining techniques became inevitable. A unique and alternative solution is to resort to

adhesively-bonded joints which can offer the capability of joining dissimilar materials with no need to introduce extra weight or weaken the structures [3]. In addition, adhesive bonding in naval ships can result in an overall structural weight reduction of ~10% which translates into ~7% savings in fuel consumption and consequently harmful emissions [4].

Although adhesive bonding and lightweight materials have gained a widespread adoption in the automotive and aerospace industries, their adoption in the maritime and shipbuilding industry has lagged behind. This can be justified in the light of the difference in the nature of the manufacturing process for these industries. In the automotive and aerospace industries, the manufacturing process is always conducted in a controlled environment with a regulated temperature and air/dust control [5,6]. On the contrary, the shipbuilding manufacturing operations are often exposed to the open air, making the manufacturing process control more challenging and the adhesive bonding more

---

susceptible to process defects. This raises general concerns and doubts regarding the reliability and repeatability of the process and the final product, which is the adhesively-bonded joint in this case. These concerns are even more justified when considering the long-term performance of such joints as they are exposed to harsh marine environment and thermal as well as mechanical fatigue loads, during their service life [7,8].

The lack of acceptance of adhesive bonding is currently limiting its application to secondary structures, whose failure is not detrimental for the structural safety [9]. For decades, the use of adhesive bonding in marine structures has been hindered with the quality of the adhesive-bonded joint as it represented the weakest link "at least conceptually" and this led to the situation that up till now there exists no standards or acceptance of adhesively bonded joints in maritime primary structural applications. In addition, most of the adhesives used are epoxy-based [1,3,8,10]. These adhesives have high modulus and high strength but on the other hand, they are relatively brittle as opposed to other non-epoxy-based adhesives [11,12]. Another important design aspect which has been the focus of previous research is the effect of the bondline thickness under mode I [10,13], mode II [14,15] and mixed mode [16] loading conditions. These studies investigated bondline thicknesses ranging from 100 μm to 10 mm, and they concluded that the estimated fracture toughness is sensitive to the change in the bondline thickness. To cope with some of aforementioned drawback, recently, the attention has been directed towards other solutions such as the MMA-based adhesives [17] especially for relatively thicker adhesive bondlines (>4 mm). Such adhesives offer a very high degree of ductility "flexibility and toughness" which is important to avoid catastrophic failure. Moreover, a very valuable advantage that such MMA-based adhesive offer is their tolerance to the manufacturing-induced defects. Such manufacturing-induced defects are very common in an industrial environment such as the maritime industry. Shipyard conditions are often contaminated with oils and dusts challenging surface pre-treatments, both, the temperature and relatively humidity are not controlled forcing low temperature curing, larger-gap filling requirement/manufacturing tolerances are required leading to void formation and varying adhesive thicknesses. To the authors knowledge, limited research has focused on such MMA-based adhesives for maritime applications [11,12,18] on all levels from the coupon level to the full-scale. Saeedifar et al. [12] classified the damage mechanisms of bi-material (steel-to-composite) adhesively-bonded joints on the sub-component level using Acoustic Emission (AE) data from the coupon level testing of the constituting materials and validated his approach against experimental, Digital Image Correlation (DIC) and Fiber Optic Sensors (FOS) results. Jaiswal et al. [18] extended the work using the same material system to investigate the performance of such adhesives on the full-scale using a 1:1 ratio U-joint representing a steel hull to a composite superstructure connection. They concluded that the interface is not the weak link in the chain, and failure occurs due to the inferior toughness of the resin system used in the composite laminates manufacturing.

This study focuses on the comparison between a benchmark epoxy-based adhesive that has been used for maritime applications and a newly introduced MMA-based adhesive. The aim of the study is to demonstrate the damage and defect tolerant capability of the MMA-based adhesives and highlight their potential in being used in marine structures for thick bondlines (~8 mm) for bi-material (composite to metal) joints. The bulk properties of both adhesives are characterized via tensile and compact tension (CT) fracture toughness tests while their interfacial mode I fracture toughness is characterized on the metal substrates, steel in this case, via a double cantilever beam (DCB) test. The objective here is to characterize the adhesive-steel interface while the adhesive-composite interface will be the subject of future work. The experimental data reported are followed by theoretical and numerical analyses.

This work is structured in the following manner. After introduction, in Section 2, the used materials and specimen preparation protocols are detailed. In Section 3 all experiments and procedures are outlined. Section 4 describes the standardized data reduction protocols and the emerging crack growth locus and crack growth kinetic relations. Three additional aspects, related to the geometry of the specimens used: the adhesive thickness effect, the mode mixity due to the interfacial crack growth, and the effect of plasticity are also emphasized. In Section 5 experimental results are disclosed and discussed in detail. Finally, Section 6 concludes the presented work.

## 2. Materials and manufacturing

2.1. Adhesives and adherends

The epoxy-based adhesive used in this study is a two-component toughened epoxy adhesive with a mixing ratio of 1:1 by volume. The adhesive tensile modulus is ~2 GPa with a tensile strength of ~30 MPa and strain to failure of 4.4% as per the manufacturer datasheet. The MMA-based adhesive used is a two-component methacrylate adhesive with a mixing ratio of 10:1 by volume. The adhesive tensile modulus is ~200 MPa with a tensile strength of ~15 MPa and strain to failure of 40–60% as per the manufacturer datasheet. For the DCB specimens, the steel used in this study was AH36 with Young's modulus of ~200 GPa, yield strength of 350 MPa, ultimate strength of (400–550) MPa and Poisson's ratio of 0.26. The thickness of the steel plate used is 6 mm.

2.2. Specimens' manufacturing

A manual gun with a mixing nozzle was used to mix and apply the two-component epoxy-based adhesive with a mixing ratio of 1:1 by volume. For the MMA-based adhesive a pneumatic gun with a mixing ratio of 10:1 by volume was used (see Fig. 1a). The thickness of the different plates was controlled by spacers to achieve ~2.6 mm for the dog-bone specimens and ~8 mm for the CT specimens for both adhesives. However, the MMA-based adhesive CT specimens experienced shrinkage during curing resulting in thickness of ~7.6 mm as opposed to ~7.9 mm for the epoxy-based counterparts. All manufactured plates were room temperature cured for 24 h then post cured at 80 °C for 1 h (see Fig. 1b). It is worth mentioning here that this post-curing step was only carried out for the adhesives' characterization cases "dog-bone and CT" not for the interfacial characterization DCB specimens as it will be explained later in this section. Afterwards, these plates were waterjet cut to the desired shape (see Fig. 1c and d). The dimensions of the dog-bone and CT specimens are depicted in Fig. 1c and d. For the CT specimens, a pre-crack was introduced using a sharp razor blade, by tapping, to have a sharp crack tip as per the standard recommendations.

As highlighted in the introduction, the motivation for this study is industry-driven and the design of the DCB specimens reflect the following requirements: i) thick bondline, ii) crack at metal/adhesive interface to force the crack to propagate along it, and, iii) curing at room temperature. In maritime applications, the bonding and curing have to be done in shipyard conditions due to size limitations and accessibility. When it comes to the surface pre-treatment, the shop primer on the steel was removed by grit blasting up to SA2.5 grade [19] which is a standard steel surfaces pre-treatment grade in maritime applications. Then, the adherends' surfaces were degreased and cleaned with isopropanol prior to bonding. Moreover, the curing of the adhesive was only a room temperature curing in the case of the DCB specimens manufacturing. All the DCB specimens had the same nominal dimensions (length x width ~ 250 mm × 25 mm) with an 80 mm long and 0.01 mm thick Teflon sheet to act as the crack initiator (see Fig. 2). All specimens were designed so that the distance between the loading pin and the initial crack tip is ~50 mm as per the ISO 25217 standard procedure. In both cases, epoxy-based and MMA-based, the adhesive was injected by a pneumatic gun at the center of two steel plates (250 × 250 mm) while maintaining the adhesive thickness (~8 mm) using spacers placed at the four edges. Once the injection is completed, the bonded plates were left for 24 h at
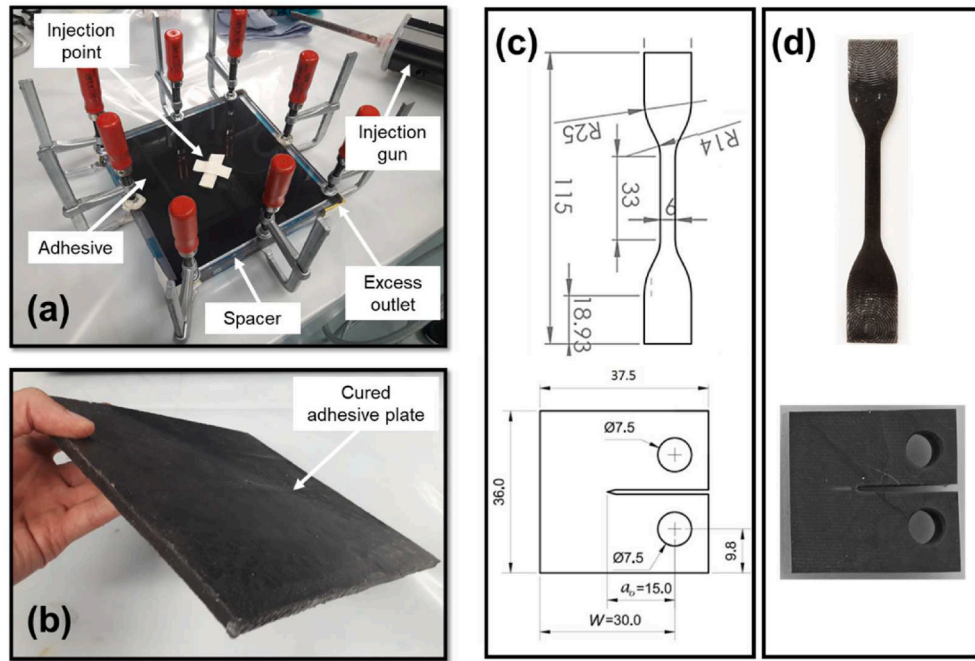
Fig. 1. The manufacturing process of bulk adhesive specimens: a) adhesive injection, b) cured adhesive plate, c) dimensions of the tensile dog-bone and CT specimens and d) representative specimens after the waterjet cutting.
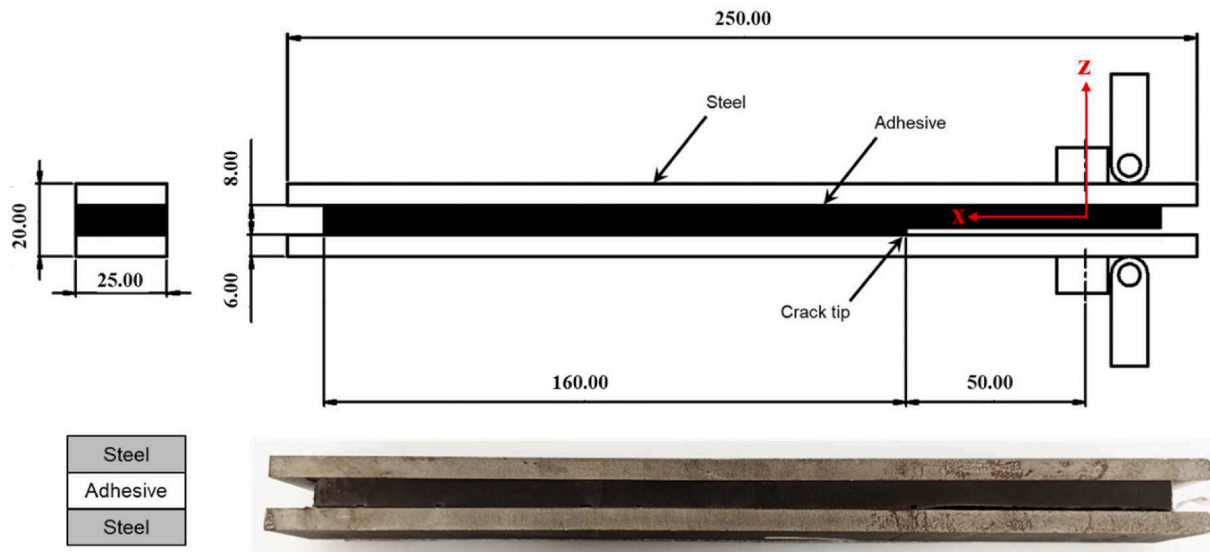
Fig. 2. DCB specimen after injection and waterjet cutting (bottom) and schematic summarizing all the dimensions in mm (top).

room temperature for curing. After that, they were waterjet cut into the DCB specimens' dimensions (see Fig. 2).

3. Experimental procedure

3.1. Adhesive characterization

3.1.1. Tensile dog-bone testing

For the tensile testing characterization of both adhesives, the ASTM D638 standard was followed. The nominal thickness of the specimens was ~2.6 mm. The test (see Fig. 3a) was carried out under displacement-controlled conditions, with a displacement rate of 1.27 mm/min. The machine used for testing was a Zwick/Roell machine equipped with a 10 kN load cell and hydraulic grips to minimize the slippage. The

machine used and the loading rate were the same for all the testing conducted in this study, not just for the tensile dog-bone testing. The applied force and the crosshead displacement were recorded by the machine during the test. Five specimens of each adhesive type were tested to ensure the repeatability and reproducibility of the results.

3.1.2. Compact tension (CT) testing

For the CT testing of both adhesives the ASTM D5045 standard was followed. The nominal thickness of the specimens was ~8 mm. Each specimen was loaded through the pins as shown in Fig. 3b. The applied force and the crosshead displacement were recorded by the machine during the test. Five repeats of each adhesive type were tested to ensure the repeatability and reproducibility of the results.
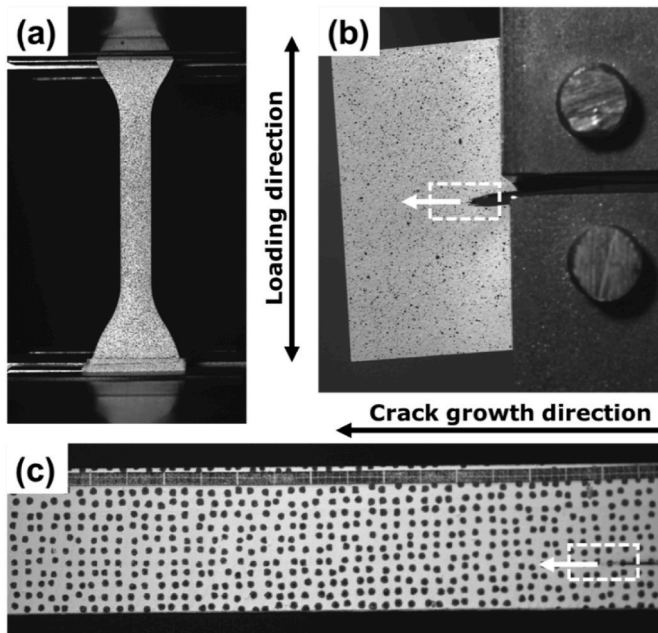
Fig. 3. Camera images showing specimens during testing with DIC speckle pattern: a) tensile, b) CT and c) DCB specimens.

3.2. Double cantilever beam (DCB) testing

The mode I fracture toughness DCB test was carried out, according to the ISO 25217 standard, using the same machine and testing conditions as both the dog-bone and the CT specimens. Three specimens for each adhesive type were tested to verify the repeatability and reproducibility of the results. A representative specimen under loading covered with the DIC speckle pattern is shown in Fig. 3c.

3.3. Digital Image Correlation (DIC)

To visualize the full field displacement map in the dog-bone tensile test and ahead of the crack tip in the case of the CT and DCB testing, a two-dimensional (2D) DIC system was used. Besides, the system was also used to measure the crack length throughout both CT and DCB tests. The DIC system consisted of a 8-bit "Point Grey" camera with a resolution of 5 MP, equipped with a "XENOPLAN 1.4/23" lens. The software used for capturing and recording the speckle pattern images was ViC-Snap 8 while post-processing was run in ViC-2D 6 software (Correlated Solutions Inc., USA). The observation window, in mm^2, and the acquisition rate, in frames per second (fps), for each testing campaign was different as detailed in Table 1.

During all the tests, analogue outputs from the testing machine were connected to the DIC system to synchronize the acquired images with the corresponding load and displacement at each point in time. This is very important for all the post-processing calculation: tensile properties, the fracture toughness as function of the load, displacement, and crack length for both CT and DCB cases.

Table 1
Summary of the DIC parameters used.

	Tensile	CT	DCB
Observation window (mm^2)	90 × 75	550 × 460	580 × 310
Acquisition rate (fps)	0.33	0.20	1.00

4. DCB analysis and mode mixity calculation

4.1. Data reduction

4.1.1. Standardized expressions for the strain energy release rate (ERR)

The two data reduction techniques to calculate the strain energy release rate G_I used here are: i) the simple beam theory (SBT) and ii) the corrected beam theory (CBT). For a detailed discussion, the reader is referred to the ISO standards [20]. The strain energy release rate G_I calculated using the SBT and CBT techniques, are given respectively as:

$$G_{I-SBT} = \frac{4P^2}{E_s b^2}\left(\frac{3a^2}{h^3} + \frac{1}{h}\right) \tag{1}$$

$$G_{I-CBT} = \frac{3P\delta}{2b(a + |\Delta|)} \tag{2}$$

where: P = applied force, E_s = substrate/adherend stiffness, h = adherend thickness, a = crack-length, b = specimen width, $\delta\delta$ = measured displacement, and $|\Delta|$ = crack-length correction. The constitutive relation between the force (P) and displacement (δ) in the initial loading linear segment in the case of SBT (neglecting shear effects) and the CBT (assuming $\Delta \to 0$), can be expressed as:

$$\delta = 8\frac{P}{E_s b h^3}a^3. \tag{3}$$

4.1.2. Power law relation for crack growth

In Eq. (2), considering that the offset Δ can be neglected, and assuming that at the crack onset the fracture criterion is met $G_{I-CBT} \to G_c$, yields $a = \frac{3P\delta}{2bG_c}$. Eq. (3) can be then rewritten for P, yielding crack growth locus:

$$P = b\sqrt[4]{\frac{1}{27}\ G_c^3 E_s h^3}\delta^{-\frac{1}{2}}. \tag{4}$$

Thus, once the crack propagates under G-controlled conditions, the following $P \propto \delta^{-\frac{1}{2}}$ scaling holds. Note that Eqs. (3) and (4) form a pair of power law relations that can be used to predict the behavior of any DCB specimen in $P(\delta)$ coordinate system.

4.1.3. DCB equation of motion

The crack growth rate is important in understanding how fast a crack propagates under given loading conditions. With Eq. (1), where the shear related $\left(\frac{1}{h}\right)$ term is dropped, i.e. $G_{I-SBT} = \frac{4P^2}{E_s b^2}\left(\frac{3a^2}{h^3}\right)$, and rearranging Eq. (3) to compliance relation $C = \frac{\delta}{P} = \frac{4a^3}{E_s b h^3} \to P = \frac{1}{4}E_s b \frac{h^3}{a^3}\delta$, the energy release rate becomes:

$$G_{I-SBT} = \frac{3}{8}\frac{E_s h^3 \delta^2}{a^4}. \tag{5}$$

Since at the fracture onset $G_{I-SBT} = G_c$ (note that under the assumptions made $G_{I-SBT} \equiv G_{I-MBT}$), the instantaneous crack position is expressed as:

$$a = \left(\frac{3}{8}\frac{E_s h^3}{G_c}\right)^{\frac{1}{4}}\delta^{\frac{1}{2}} = c_1\delta^{\frac{1}{2}}. \tag{6}$$

The crack growth kinetics is given by Ref. [21]:

$$\dot{a} = \frac{da}{dt} = \frac{da}{d\delta}\frac{d\delta}{dt} = \frac{1}{2}c_1\dot{\delta}\delta^{-\frac{1}{2}}. \tag{7}$$

Finally, since in the displacement rate-controlled experiments $\dot{\delta} = const.$ for the DCB configuration, the crack growth rate can be expressed through:

$$\frac{da}{d\delta} = \frac{1}{2}c_1\delta^{-\frac{1}{2}}. \tag{8}$$

Eq. (8), outlining another power law relation, will be referred to as the crack growth rate expressing how far the crack can propagate under a unit of applied displacement.

4.1.4. Generalization of energy release rate to account for plasticity – criterion for crack growth self-similarity

The total potential energy Π that takes into account steel adherend, with the bondline is only represented through G_c, can be represented, in the light of the variational formulation and the energy balance, as:

$$\Pi = \int_V U_{el} dv + \int_V U_{pl} dv + \int_\Gamma G_c dA - \int_{\partial V} t_i u_i dA \tag{9}$$

where $U_{el} = \frac{1}{2}\sigma_{ij}\varepsilon_{ij} \approx = 2\frac{P^2 a^3}{E_s bh^3}$ $(i,j = x, y, z)$ is the stored elastic strain energy, U_{pl} is the plastic energy, V is the volume of the steel adherends from the point of load application to the crack tip, Γ is the created crack surface, dA denotes area operation, ∂V is the area of the boundary spanning over V, the term $\int_{\partial V} t_i u_i dA = \int_\Delta P d\delta$ is the work of external forces, and equivalently the area under the force-displacement curve. Taking the first variation with respect to the growing crack as a functional minimizer:

$$\frac{d\Pi}{da} = \frac{2}{3}\frac{P^2 a^2}{E_s bh^3} + \frac{d}{da}\int_v U_{pl} dV + G_c b - \frac{d}{da}\int_\Delta P d\delta = 0 \tag{10}$$

and thus:

$$\left(\frac{d}{bda}\int_\Delta P d\delta - \frac{2}{3}\frac{P^2 a^2}{E_s b^2 h^3} - G_c\right) = \frac{d}{bda}\int_v U_{pl} dV. \tag{11}$$

One can rapidly verify that for the elastic case equality provided by eq. (11) reduces to 0 ($\frac{d}{bda}\int_\Delta P d\delta \to \frac{2}{3}\frac{P^2 a^2}{E_s b^2 h^3}$, and $\frac{d}{bda}\int_v U_{pl} dV = 0$). All the previously derived fracture scaling laws, i.e. eqs. (4), (6)–(8) as well as eqs. (1) and (2) are deduced from this case. However, the same scaling laws could be obtained considering that the adherend undergoes plastic deformation at some stage of the crack growth. The condition for that to hold true is:

$$\frac{d}{da}\left(\frac{d}{bda}\int_\Delta P d\delta - \frac{1}{2b}\frac{P^2 a^2}{E_s I} - G_c\right) = \frac{d}{da}\left(\frac{d}{bda}\int_v U_{pl} dV\right) = 0 \tag{12}$$

and so, both sides of the energy balance given by eq. (11) can either change at the same rate or need to remain constant during crack growth. Eq. (12) formulates the general criterion for the steady-state (dynamic events are not considered) and self-similar crack growth (constant energy flux in the system) in the presence of plastic deformation of the adherend. Note that from eq. (12), one elucidates that $\frac{d}{bda}\int_v U_{pl} dV = const.$ during the crack growth, and thus, the associated adherend damage zone size is fixed. Based on eq. (12), the following cases/scenarios can be theorized to occur during testing the DCB specimens:

- Elastic-perfectly plastic or elastoplastic with softening adherends: In this case, a plastic hinge will be created near the crack tip region and the evaluation of the adhesive properties will not be possible as the adherend will flow until fracture.
- Elastoplastic with hardening adherends
  o adherends undergo plastic deformation incl. hardening but with the failure strains insufficient to reach energy of fracture threshold of the adhesive: Adherend will harden but fail due to fracture. Fracture characterization of the adhesive not possible.
  oadherends undergo plastic deformation incl. hardening but with failure strain sufficient to attain fracture threshold of the adhesive: Loading beyond the adherend yielding stress allows the material to harden near the crack front region. This ensures an

increase in the amount of the energy stored until the fracture energy in the adhesive is reached as stated by eq. (11). Upon onset of the steady-state and self-similar crack propagation, the stresses inside the adherend do not increase nor decrease and the stiffness of the material E_s can be regarded as unaffected – thus, the criterion stated through eq. (12) is satisfied.

4.2. Effect of adhesive thickness

The SBT assumes that the bonded region is infinitely stiff and thus neglects the fracture process zone effect ahead of the crack resulting in a zero-crack tip opening displacement and root rotation. Due to the finite stiffness of the adhesive and non-negligible thickness, the adherends cannot be treated as completely fixed at the crack tip. In addition, neglecting adhesive layer implies non-existence of stress and strain fields. Considering thick, obeying Hooke's law, bondlines with modulus E_a and Poisson's ratio ν_a, stresses (σ_{ij}) and strains (ε_{ij}) can expressed, in the light of continuum mechanics, as:

$$\sigma_{ij} = \frac{E_a}{1+\nu_a}\left[\varepsilon_{ij} + \left(\frac{\nu_a}{1-2\nu_a}\right)\varepsilon_{kk}\delta_{ij}\right] \tag{13}$$

$$\varepsilon_{ij} = \frac{1}{E_a}\left[(1+\nu_a)\sigma_{ij} - \nu_a\sigma_{kk}\delta_{ij}\right] \tag{14}$$

respectively. Here, i, j, k are related to the displacement field and can take values x, y, z and δ_{ij} is Kronecker's delta. Einstein summation applies over k. During the DCB test, the main load acting on the bondline comes from the varying deflection $\delta(x)$ along the bonded region. Thus, the main stress and strain components ($i, j = z$) are respectively:

$$\sigma_{zz} = \frac{E_a}{1+\nu_a}\left[\frac{\varepsilon_{zz}(1-\nu_a)}{1-2\nu_a} + \left(\frac{\nu_a}{1-2\nu_a}\right)\varepsilon_{xx} + \left(\frac{\nu_a}{1-2\nu_a}\right)\varepsilon_{yy}\right] \tag{15}$$

$$\varepsilon_{zz} = \frac{\sigma_{zz}}{E_a} - \frac{\nu_a(\sigma_{xx} + \sigma_{yy})}{E_a}, \tag{16}$$

However, other components arise due to the finite value of ν_a. While the objective of this work is not to propose detailed analysis, to correctly interpret results considering thick and soft bondlines, Poisson's ratio effects outlined by eqs. (15) and (16) should be acknowledged as they become non-negligible at the bondline scale under consideration.

4.3. Mode mixity

Due to the non-negligible bondline thickness ($\sim$8 mm) and the pre-crack being introduced at one of the adhesive-substrate interfaces, asymmetric loading acting at the crack tip can be expected. This may have direct effect on the fracture toughness mode being evaluated by this DCB test. Thus, finite element model with embedded virtual crack closure technique (VCCT) was formulated in ABAQUS Standard 3DEX-PERIENCE R2017x and used to simulate the DCB specimen and find out the mode mixity ratio due to this asymmetric design at the crack tip. The model was used to simulate the steel-to-steel bonded DCB specimen with a bondline thickness of 8 mm and steel thickness of 6 mm. The initial crack length was set to 50 mm, and the boundary conditions were specified to resemble the DCB testing boundary conditions by having a displacement applied at the upper loading pin and allowing only rotation around the centerline of the lower pin. The model was meshed with element type C3D8R: a 8-node linear brick, reduced integration, hourglass control element, resulting in approximately 150k nodes for 125k elements. Fig. 4 shows the energy release rate ratio distribution for both mode I and mode II across the crack front as predicted by the simulation. The geometrical asymmetry resulted in a dominant Mode I ($>$95%), rather than a pure mode I, with a very slight difference between the epoxy-based and the MMA-based adhesives. This suggests that the adherend bending rigidity effect is more significant than the adhesive properties as long as the adherends remain the same. Indeed, this can be
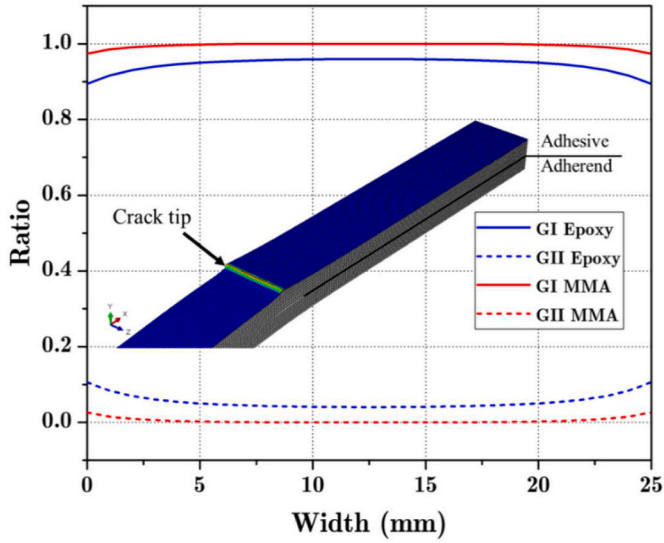
Fig. 4. The energy release rate ratio across the DCB specimen's width plotted along the crack tip. Note: The top adherend is removed to show the location of the crack tip at the interface.

proven also by introducing lamination theory. For the steel adherends of thickness h covered by adhesive layer of thickness t (so that the total bondline thickness is $2t$) and modulus E_a then the bending rigidity of such laminate is generalized [22]:

$$EI_{eff} = \frac{b}{12} \frac{\left[E_s^2 h^4 + E_a^2 t^4 + E_s h E_a t \left(4h^2 + 6ht + 4t^2\right)\right]}{E_s h + E_a t}. \quad (17)$$

Based on the calculations of the assumption in eq. (17), the difference between the bending rigidity of both scenarios (MMA-based vs. epoxy-based) is found out to be less than 5%. This is in a very good agreement with the VCCT results confirming the conclusion that the adhesive properties effect is negligible compared to the geometry effect. But also, this is due to the fact that the epoxy and MMA-based adhesives' moduli are two and three orders of magnitude less than the steel, so their effect on the bending rigidity and mode mixity is negligible and even with such asymmetric DCB specimen design, the dominant mode remains mode I.

5. Results and discussion

5.1. Adhesive characterization

5.1.1. Tensile dog-bone testing

A representative stress-strain curve for the two adhesives is depicted in Fig. 5a. As it can be seen, the epoxy-based adhesive is much stiffer than the MMA-based, with a relatively high strength and low strain to failure. For the MMA-based case, the lower strength and stiffness are compensated by the ductile nature of the adhesive leading to almost 40% strain to failure and equivalently higher energy absorbed up to failure. In both cases, the failure occurred within the gauge length of the specimen as highlighted by the strain concentration in the DIC images (see Fig. 5b and c) taken before the final failure. For the sake of comparison, the key mechanical properties are summarized in Table 2.

5.1.2. CT testing

For the CT specimens, a representative load-displacement curve for each adhesive type is shown in Fig. 6a along with the normal strain (ε_{zz}) at the crack-onset. In a very similar manner to the tensile dog-bone tensile results, the epoxy-based adhesive response appears much stiffer as opposed to the MMA-based with almost double the maximum load (~145 N) but on the contrary only 20% of the displacement to failure (~1.5 mm) of the MMA-based adhesive. This again highlights the different nature of both adhesives in the sense of stiffness/strength versus ductility/toughness. In addition, the DIC images (see Fig. 6b and c) capture the strain map ahead of the crack tip and confirm the fact that much higher strains/strain energies are required for the existing initial crack to grow/propagate. Moreover, for the sake of comparison, the plastic zone envelop is highlighted by the black arrows on the DIC images (see Fig. 6b and c). Considering the same iso-strain closed contour for both cases, the area ratio of the zone for the MMA-based adhesive is found out to be more than 3.5 times larger than the epoxy-based counterpart.

When it comes to the energy release rate calculations, the difference

Table 2
Summary of the tensile properties of the epoxy-based and MMA-based adhesives.

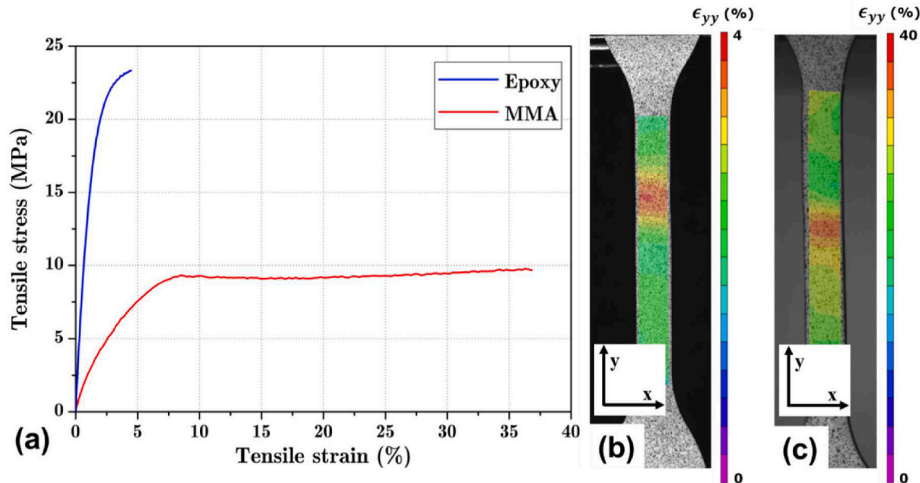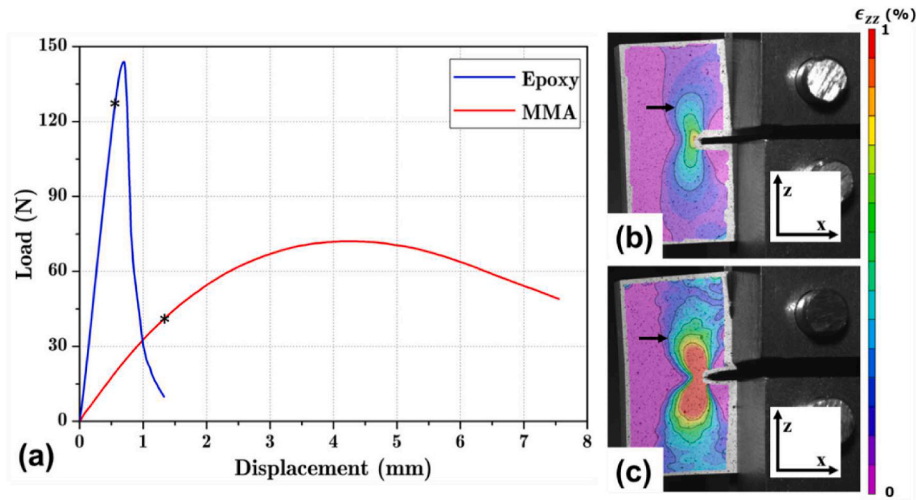|	Tensile modulus (MPa)	Maximum stress (MPa)	Failure strain (%)	Poisson's ratio
Epoxy	1717.28 ± 89.18	23.50 ± 1.22	4.34 ± 0.73	0.33 ± 0.00
MMA	258.11 ± 17.83	9.83 ± 0.41	35.58 ± 7.62	0.46 ± 0.01

Fig. 5. Representative tensile: a) stress-strain curves, b) epoxy-based adhesive strain map and c) MMA-based adhesive strain map just before the final failure.

Fig. 6. Representative CT: a) load-displacement curves, b) epoxy-based adhesive strain map and c) MMA-based adhesive strain map at the crack-onset moment (marked with * on curves).

between the two adhesives in their nature and response requires further attention. According to the ASTM D5045, one of the main validity checks to be able to use the Linear Elastic Fracture Mechanics (LEFM) within the CT data reduction and the energy release rate calculations is the ratio of the maximum load (P_{max}) to the critical load (P_Q) at which the crack starts to propagate ($P_{max}/P_Q \leq 1.1$). This is valid for the epoxy-based adhesive (~1.04) but not valid for the MMA-based adhesive case (~2.63). Thus, the decision has been made in the following discussion to resort to the *J*-integral approach in order to be able to accurately determine both the elastic and the plastic components of energy.

The elastic stress intensity factor (K_i) for a CT specimen, at a point *i* on the load-displacement curve, is defined as:

$$K_i = \frac{P_i}{B\sqrt{W}} f\left(\frac{a_i}{W}\right)$$ (18)

where: P_i = applied load at point *i*, a_i = crack length at point *i*, W = specimen width, B = specimen thickness, and $f\left(\frac{a_i}{W}\right)$ = geometry function as detailed in ASTM E1820.

The elastic component of the *J*-integral (J_{el}) is thus calculated as function of the stress intensity factor as:

$$J_{el} = \frac{K^2(1 - v^2)}{E}$$ (19)

where: E = tensile modulus, and v = Poisson's ratio. In the case of ductile polymers/adhesives, the elastic component of the *J*-integral is not the only component that contributes to the strain energy for a cracked specimen under mode I. Thus, the plastic component (J_{pl}) should also be calculated as follows [23]:

$$J_{pl} = \frac{\eta_{pl} A_{pl}}{B b_0}$$ (20)

where: A_{pl} = area under the load-displacement curve as detailed in Refs. [23,24], b_0 = un-cracked ligament ($W - a_0$), B = specimen thickness, and $\eta_{pl} = 2 + 0.522\, b_0/W$.

For the CT specimen, the total *J*-integral is the summation of the elastic and plastic components:

$$J = J_{el} + J_{pl}.$$ (21)

Table 3 gathers estimations of resistance to fracture obtained through eqs. 18–21 along with ratio between MMA and epoxy adhesives properties.

The elastic, *K* based measures, related only to the measured P_i,

Table 3
Summary of the CT results of the epoxy-based and MMA-based adhesives at maximum load.

|	K (MPa.m$^{1/2}$)	J_{el} (kJ/m^2)	J_{pl} (kJ/m^2)	J (kJ/m^2)
Epoxy	38.12 ± 0.25	0.71 ± 0.01	0.19 ± 0.01	0.90 ± 0.01
MMA	18.91 ± 0.36	1.09 ± 0.04	2.42 ± 0.17	3.51 ± 0.17
MMA/Epoxy	0.49	1.54	12.74	3.9

indicate that the resistance to fracture of MMA adhesive is approximately half of the epoxy adhesive. Nevertheless, including plasticity, associated with the volume over which the energy is dissipated, suggests that MMA is almost 4x tougher. From design and safety perspectives such difference must be considered.

5.2. DCB fracture testing

5.2.1. Load-displacement curves and direct observations

Fig. 7 shows the load-displacement curves for the epoxy-based DCB specimen and the experimentally captured crack propagation using the DIC camera. As shown by the images (see Fig. 7b), the crack propagation at the three designated points (1, 2 and 3) is gradual with no abrupt jumps occurring at the surface although the macroscopic load-displacement curve of this specific representative specimen has some local peaks. In addition, the crack path for all the epoxy-based specimens is found to be repeatable in the sense that it starts from the interface where it was artificially designed, propagates in an inclined direction and settles in the middle of the adhesive layer. This can be explained by the asymmetric nature of the DCB specimen. There exists a shear stress component that drives the crack away from the interface at the beginning up to the point at which the dominant mode is only mode I opening. Once the crack reaches this plane corresponding to pure mode I loading state, it continues propagating along the same plane. This clearly indicates that the quality of the interface is not the weakest link as the failure is apparently cohesive failure within the adhesive.

Fig. 8 shows the load-displacement curves for the MMA-based DCB specimen and experimentally captured crack propagation using the DIC camera. The images at the three designated points (1, 2 and 3), reveal a quite different crack propagation of the MMA in comparison with the epoxy-based. At a far sight, an apparent crack onset occurs close to the interface. It is a bit difficult to observe any sudden jump in the crack propagation path that might have led to any sudden drops in the load-displacement curve. However, in zoomed-in image it can be observed that the crack is not propagating across the entire specimen width. Just
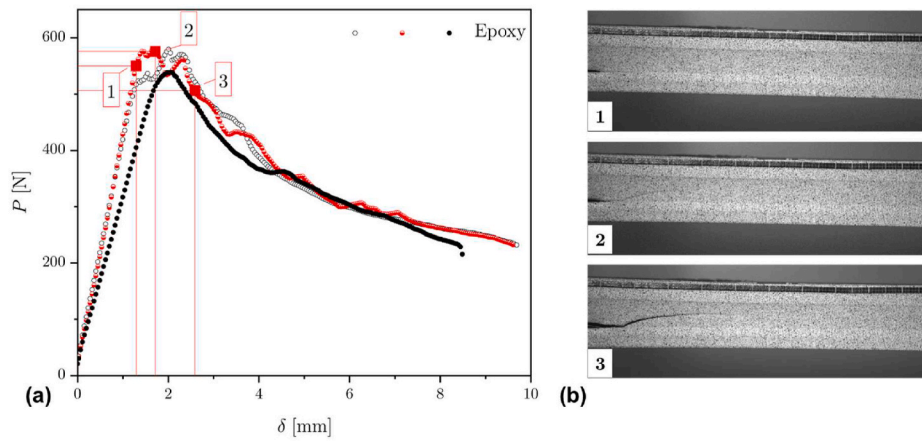
Fig. 7. Results obtained during DCB experiments with epoxy-based bondline. a) Load–displacement curves and (b) experimentally measured crack lengths using DIC camera.
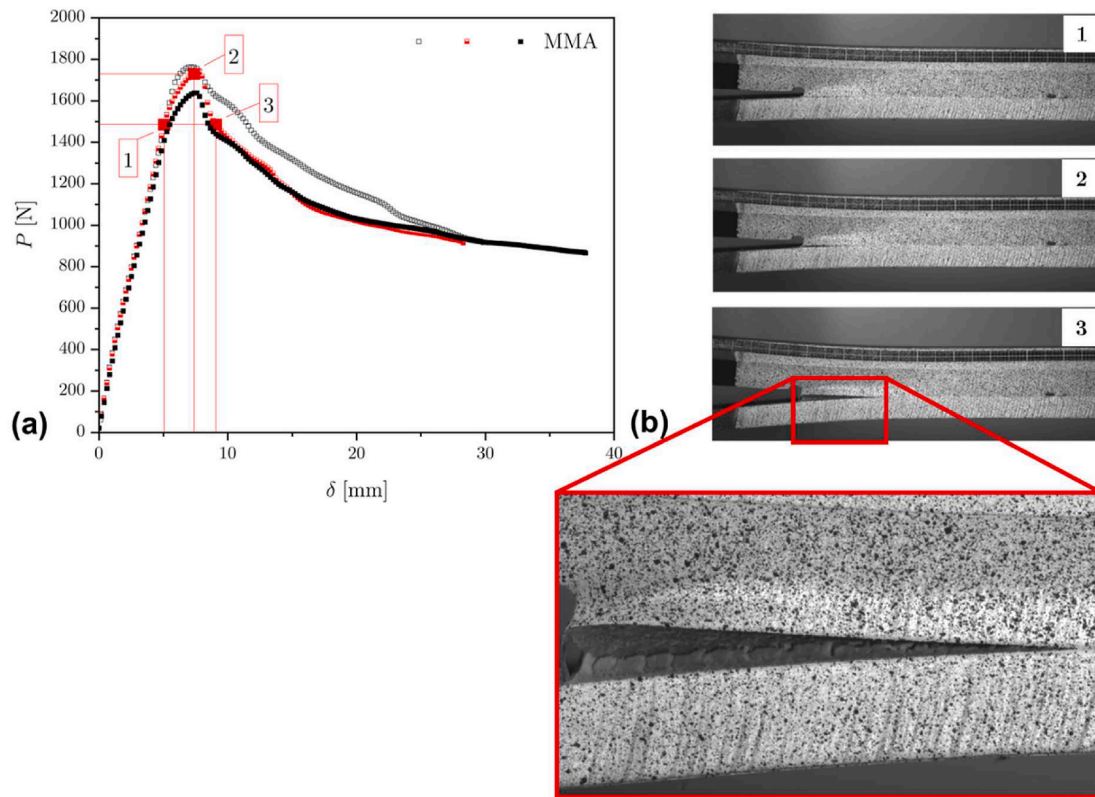

Fig. 8. Results obtained during DCB experiment with MMA-based bondline. a) Load–displacement curves and (b) experimentally measured crack lengths using DIC camera. In addition, the inset close-up on the region near the interface. The apparent crack propagates along the MMA/steel edge but not across the entire DCB specimen's width.

behind the crack, adhesive remains un-fractured.

To better understand the fracture phenomenon in both adhesives, the 2D-DIC strain fields inside the process zone are analyzed. At first, in Fig. 9(a–f) the epoxy-based system is investigated with columns corresponding to the three points indicated in Fig. 7, and rows reflecting ε_{xx} and ε_{zz}. Observations show that the stress-strain field is highly affected by the Poisson's ratio eq. (15) and eq. (16). While, due to the out-of-plane Poisson's ratio related effects, the 2D-DIC is not fully reliable quantitatively, the color codes are chosen such that maximum strains results in $\nu_{xz} = -\frac{\varepsilon_{xx}}{\varepsilon_{zz}} \approx 0.32$; the value expected for such epoxy adhesives in their elastic state. At the crack onset, Fig. 9 (a) and (d), the major component is ε_{zz} as expected, with a compressive zone ahead of the

crack. Significant through-adhesive-thickness strain variation is reported revealing how the adhesive thickness affects the local distributions of strains and thus stresses. Once the crack deflects away from the interface, Fig. 9 (b) and (e), the crack tip stress-strain field takes the characteristic shape for the plane-stress conditions. This is expected, as only the side of the specimen is visible. The crack then propagates with the crack tip stress state remaining self-similar, see Fig. 9 (c) and (f). During the entire self-similar crack growth stage, the through-the-thickness variation remains unchanged and is constrained by the bondline thickness – the radius of the fracture process zone exceeds thickness of the adhesive layer. The same applies to the compressive stresses ahead of the crack tip propagation taking place along the
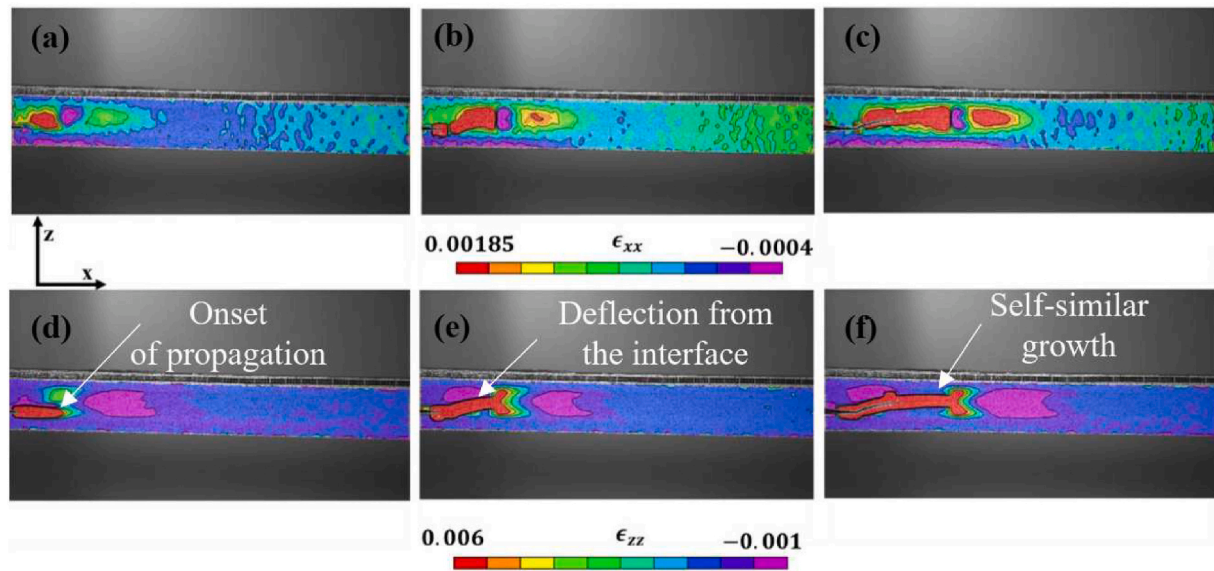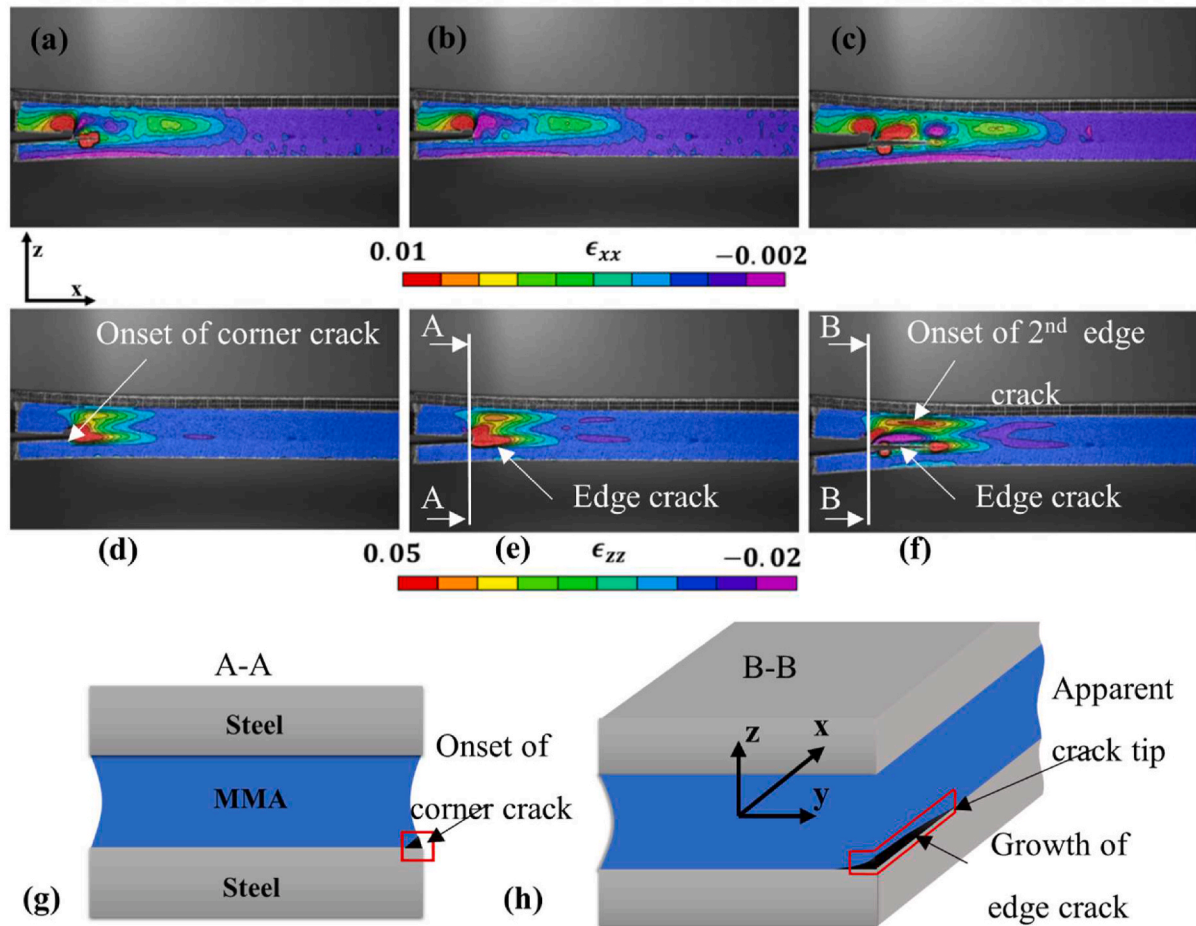
Fig. 9. 2D-DIC results for the DCB specimen with epoxy-based adhesive. Columns corresponds to the three points indicated in Fig. 11. Rows reflects ε_{xx} (a–c) and the corresponding ε_{zz} (d–f) components of strain field. Total thickness of specimen is 20 mm.

specimen symmetry plane [25].

Similar quantities as in Fig. 9, but for the DCB specimens with MMA adhesive are depicted in Fig. 10. Here, columns, (a, d), (b, e) and (c, f)

correspond to the points indicated in Fig. 8. Both ε_{xx} (a-c) and ε_{zz} (d-f) strain components measured from the side are presented. In the MMA adhesive case, due to significant Poisson's ratio effects and multiple

Fig. 10. 2D-DIC results for the DCB specimen with MMA-based adhesive. Columns corresponds to the three points indicated in Fig. 18. Row (a–c) reflects ε_{xx} and (d–f) ε_{zz} components of strain field. The last row includes schematic representation of the crack front/damage region view detailing the major cracking processes taking place including onset of propagation (g) and subsequent growth of the edge crack (h).
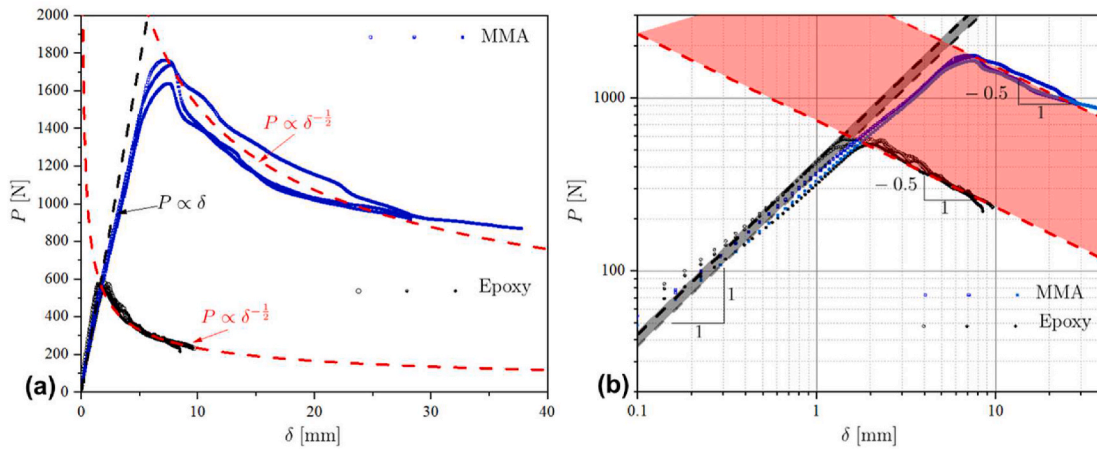
Fig. 11. Force – displacement curves summarizing DCB experiments. (a) Results plotted in the double-liner scale. (b) Results plotted in double-logarithmic scale outlining very good agreement with linear-elastic scaling laws.

phenomena observed, the color bars are chosen for the best data presentation and are an order of magnitude higher than the one of the epoxy system. The fracture onset (at the bondline corner), Fig. 10 (a) and (d), which is schematized in Fig. 10. (g), reveals the striking size of the deformed zone ahead of the crack as emphasized by ε_{xx}. The measured length over which non-zero strain could be detected is spreading over more than half of the depicted region equating to almost 50 mm. This naturally gives rise to ε_{zz} component and is related through eq. (14) with ε_{xx}. Once the crack begins to propagate, Fig. 10 (b) and (e), the observed characteristic plane-stress field shape for the epoxy system is not reproduced. Instead, ε_{zz}, and thus the corresponding stress component, are concentrated along both of the MMA/steel interfaces, with peak values close to the lower interface. At the interfaces, the high steel-MMA mechanical properties difference leads to the apparent crack growth along the edges, e.g., Fig. 10 (b, e) → Fig. 10 (c, f). However, this crack growth does not span across the entire specimen width. Instead, as can be observed from the zoom in picture of Fig. 8, the two steel adherends remain bonded over the majority of the specimen width. Such situation is schematically presented in Fig. 10 (h) where the crack propagation is depicted along the bottom edge as per DIC Fig. 10 (f). As visible in Fig. 10 (c) and (f), the red "high strain regions" occur along both, the bottom and the upper, edges – it is referred to them as the edge crack and the onset of the second edge crack respectively. Between these two highly strained regions, as well as in the front and behind them, the strain field visibly varies in terms of components and direction (both tensile and compressive strains from both components are visible).

As can be seen in the inset of Figs. 8, and 10 (h), the apparent crack length can be misleading as it reflects only the visible edge crack and cannot be regarded as the unique estimate of the crack length. The region between the specimen edges spreading above the apparent crack remains highly strained. With the onset of the corner crack and the subsequent growth of the edge crack [Fig. 10 (a, d) → (b, e) → (c, f)], the region above the edge crack become unloaded (stress free). As this is the case, provided that the remaining part of the joint along the specimen width is still bonded and under loading, and taking into account the Poisson's ratio action, this leads the unloaded portion to move out-of-plane of the DIC observation. This is demonstrated in the form of the negative component of strain as recorded by the DIC system as seen in Fig. 10 (f). A better description of such complex damage process can be provided through 3D image correlation, but preferably through in-situ X-ray Computed Tomography (CT) or other 3D technique enabling observation of all the phenomena taking place inside the fracture process zone. Finally, an important remark that applies only to the MMA-based case: post-mortem observation revealed that the steel adherends experienced permanent plastic deformation during testing. Following the data reduction derivations in Section 4.1, including the

generalization of energy release rate to account for plasticity, this aspect and others from the load-displacement response are analyzed in the subsequent subsections.

5.2.2. Load response and fracture power laws

Fig. 11 summarizes the load-displacement data obtained from the DCB tests of both adhesives presented in double-linear (a) and double-logarithmic (b) scales. The predicted load-displacement relations, described in section 4.1.1 to 4.1.2, of ($P{\propto}\delta$) for the initial linear part and ($P{\propto}\delta^{-1/2}$) for the crack growth are compared with the experimental data. For elastic materials, eq. (3) yields a simple linear relation between force and displacement ($P{\propto}\delta$) for the initial linear part. Such a law fitted to the initial linear part is plotted as a bold-dashed-black line in Fig. 11. Any deviation from this linear relation is deemed to originate from a non-linear material behavior, i.e., damage of either the adhesive or the adherends.

Inspecting Fig. 11a, few differences are noticed between the two sets of data obtained for the epoxy- and MMA-based bonded specimens in the form of: the macroscopic response, the maximum load, and the end-of-test displacement. Inspecting Fig. 11b, perfect agreement with the linear power-law is initially observed indicating that during initial loading both joints respond elastically $\delta \sim (0, 1)$ mm. The effect of the adhesive stiffness on the DCB specimen compliance should be minimum/negligible, especially when the adherends are much stiffer than the adhesive and only a small offset between the epoxy and MMA data is visible in Fig. 11b, represented by the back dashed region. For both cases the slope is almost the same and constant over a considerable displacement range, i.e., for epoxy within $\delta \in (0, 1.5)$, and for MMA $\delta \in (0, 2)$ mm. Before the maximum force is reached, deviation from the linear force law is observed. This stage is relatively short for epoxy-based adhesive system $\delta \in (1.5, 2.4)$, however, it is significantly longer for the MMA-adhesive specimens $\delta \in (2, 8)$ and thus, significant damage prior to the crack growth occurred. The maximum force in the case of the epoxy-based adhesive corresponds to $P \sim 580$ N (at $\delta \sim 2$ mm) and is approximately one third of the MMA-based counterpart, $P \sim 1650$ N (at $\delta \sim 8$ mm). Once the maximum force is reached, a self-similar crack growth process takes place and the load-displacement curve follows the power law of eq. (4), where $b\sqrt[4]{\frac{2}{27} G_c^3 E_s h^3} = const.$ has been fitted to the experimental data. The derived crack growth scaling law, eq. (4), implies that the fracture process zone remains unchanged in terms of the amount of dissipated energy during the crack growth process. Similitude in behavior between the two adhesives is striking in Fig. 11b with a very good agreement between the experimental data and the power-law predicted by eq. (4). This implies that the theoretical development of Section 4.1.4 on the criterion for crack growth self-similarity taking into

account plasticity holds for the MMA adhesive, i.e., eq. (12) is satisfied for the experimental results. Finally, the DCB epoxy-based specimens are completely separated at an average crosshead displacement of ~10 mm while on the contrary for the MMA-based specimens, full separation did not occur until $\delta = 40$ mm at which tests were aborted.

5.2.3. Crack growth rate

In Fig. 12, the crack length versus displacement is plotted in double-logarithmic scales for all the tested specimens. Note that eq. (6) can be equivalently written as $\log a = \log c_1 + \frac{1}{2}\log \delta$ and hence, in a double-logarithmic scale, the steady-state crack grows linearly with δ (and equivalently with time, as testing conditions are those of constant separation rate) with the slope of $\frac{1}{2}$ and the offset equating to $\log c_1 = \frac{1}{4}\log\left(\frac{3}{8}\frac{E_s h^3}{G_c}\right)$.

Two approaches are used to evaluate experimentally the instantaneous crack length a: i) an effective crack length a_{eff} and ii) an apparent crack length a_{app}. The effective crack length is determined from eq. (3), i.e. $a_{eff} = \sqrt[3]{\frac{1}{4}\frac{\delta}{P}E_s bh^3}$ using the measured experimental compliance $\frac{\delta}{P}$. Such data are represented with small, hollow, geometric symbols. The apparent crack length a_{app} is the one observed and measured from the side of the specimen following [20], and it is indicated with big, filled, symbols. For both adhesives, the data for the initial loading stage, are constant, i.e., horizontal lines, due to constant $\frac{\delta}{P}$, and such data are vastly omitted for clarity. Three stages can be identified and highlighted: i) linear loading, ii) non-linear damage and iii) steady-state crack growth for the epoxy-bonded system, and the latter two for the MMA system. In addition, the crack growth power-laws obtained through the least square fitting of eq. (6) are also plotted as dashed, bold, red line for a_{eff}, and black line for a_{app}. The shaded bands spanning along the power-law indicates 95% confidence interval.

In Fig. 12a, for the epoxy-based adhesive, a very good agreement is found between the experimental data and the steady-state crack growth power-law. For the epoxy-based bondline, only small fluctuations inside the 'damage' stage are observed. In addition, this non-linear regime is relatively short, and spreads for $\delta \in (1.5, 2.4)$ even though the logarithmic scale makes the region clearly visible. The apparent crack length data follows similar trends; however, it appears at lower values of a with a constant offset between a_{eff} and a_{app}.

The situation looks different once considering the MMA-based adhesive (see Fig. 12b). In this case, the non-linear behavior in the damage region is visible for both a_{eff} and a_{app}. The deviation from the power-law in this region is significant, and a clear transition from initial 0 slope trend to the expected power-law can be observed. Once the damage stage ends, the scaling law is perfectly recovered (the coefficient of

determination R^2 was found to be above 99% for the crack-growth region). Following the criterion given by eq. (12), in the present case, during crack growth the damage zone size remains unchanged, and the crack propagation can be considered as driven by the elastic strain energy released from the steel adherends. Compared with the epoxy-based bondline, a significant offset is captured between the effective and the apparent crack positions. For both adhesives, this offset corresponds to the length of the fracture process zone (ca. 10 and 50 mm for epoxy and MMA respectively as observed in the DIC images) and indicates that the knowledge of both, the crack position and the length of the fracture process zone, is necessary to correctly analyze the fracture process in joints with thick and flexible bondlines.

The crack growth rate results for both bondlines are depicted in Fig. 13. As the crack growth rate involves the local derivative $\frac{da}{d\delta}$, it is very sensitive to the non-linear behavior but also to the potential signal noise (e.g., electric noise affecting measurements, or uncertainty of measurement). To evaluate the crack growth rate from the experimental results, the discreet form of the derivative must be calculated viz. e.g., forward difference $\frac{da}{d\delta} = \frac{a_{i+l} - a_i}{\delta_{i+l} - \delta_i}$. Here i is the order number, while l indicates the step size. In general, the size of the step l should be as small as possible not to lose the local crack rate information, however it must be big enough not to include any electric noise and uncertainty that can lead to non-physical estimations. In this study, a step size $l = 1$ is used for the crack rate expressed through the apparent crack length measurements, and $l = 100$ for the effective crack length-based estimation. Due to the power-law nature of eq. (8) double-logarithmic scale is preferred for the presentation.

From the comparison between the epoxy-based (Fig. 13a) and MMA-based (Fig. 13b) cases, the crack propagation speed for the MMA-based is found to be almost one order of magnitude lower than its epoxy-based counterpart. The reproducibility of the results for each set of specimens verifies that the trend is consistent, and it is only due to the different nature of both adhesives and their interaction with the steel adherend interface. Moreover, this highlights the advantage of using the MMA-based adhesive over the epoxy-based counterpart in slowing down the crack speed/growth rate. This can be also attributed to the difference in the energy dissipation mechanisms between these two adhesives. In the case of the MMA-based adhesive and due to its relatively ductile nature, there exists a competition between two different energy dissipation mechanisms: the energy dissipated in the form of adhesive plastic deformation and the energy dissipated in creating "a new fracture surface" in the form of the crack growth process. This phenomena was recently reported and analyzed by Tao et al. [26] in the light of introducing crack-arrest features in DCB specimens by controlling the interfacial heterogeneity. In other words, energy is dissipated in the build-up process of the fracture process zone (FPZ) ahead of the crack tip up to a
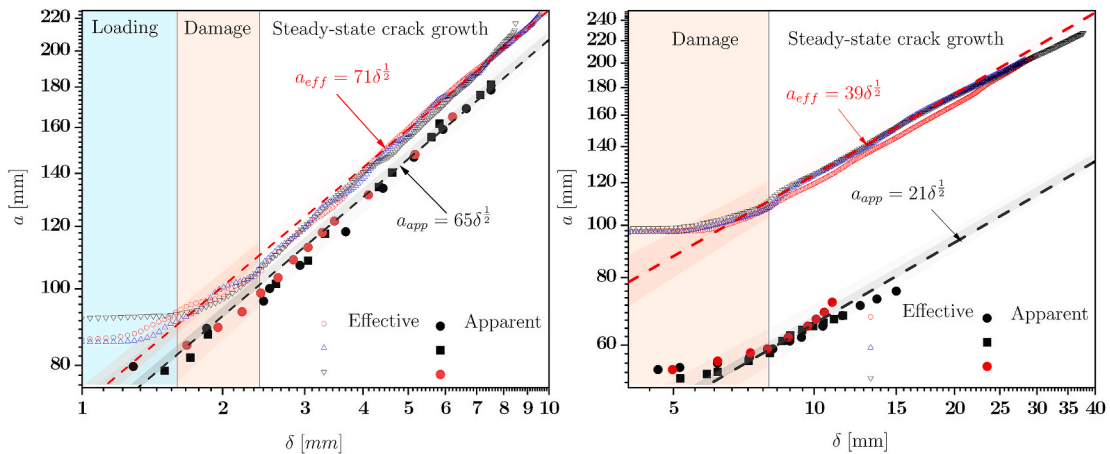

Fig. 12. Crack growth of the (a) epoxy-bonded, and (b) the MMA-bonded DCB specimens.
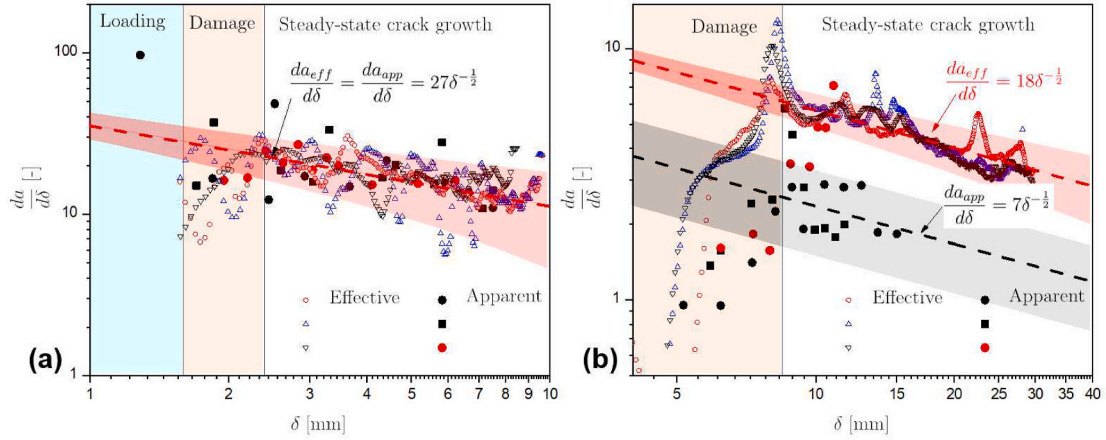
Fig. 13. Crack growth rates obtained for DCB specimens with (a) elastic-brittle epoxy, and (b) ductile MMA adhesives. Both, effective and apparent crack length cases are presented.

specific threshold above which the energy dissipation mechanism changes to creating a new fracture surface by growing the existing crack. This is shown in Fig. 13b within the damage stage where the crack rate is greater than zero, i.e., crack grows but deviates from the predicted power law, where the crack grows solely on fracture energy. Note that such damage process has its representation in both the apparent and the effective behavior. During visual inspection the crack is observed to propagate in the vicinity of the specimen edges but not along the entire specimen width as detailed before in Fig. 8. The edge cracking is due to significant Poisson's ratio effects and material gradient near the edges. Thus, for the MMA adhesive the damage is due to the internal, volumetric dissipation due to plasticity (or visco-plasticity) and due to multiple crack onset sides creating new surfaces. Unambiguous definition of the apparent crack length is impossible and relying on only the side observation is insufficient. In that manner, the a_{eff} gives a better representative phenomenological description. Damage leads to an increase of the system compliance (softening), and thus the effective crack position is expected to be larger than the apparent. As can be observed, this process appears in the crack rate graphs as rather complex, and at least two phenomena have been recognized during experiments, interlinked with the internal material damage (plasticity): plastic deformation of steel adherend and the associated crack growth from specimen edges. An important remark to note is that once damage stage is finished, the energy release rate becomes dominant, and the process of crack growth unfolds as expected according to eq. (8).

In the case of the epoxy-based adhesive, the contribution of energy dissipated by the plastic deformation of the adhesive is not as significant, leading to a faster crack growth as previously highlighted in Fig. 12. Note that for this adhesive, and in general for elastic-brittle systems $\frac{da_{eff}}{d\delta} = \frac{da_{app}}{d\delta}$. Thus, while $a_{eff} > a_{app}$, the crack growth rate remains the same. For adhesives like MMA, in which the fracture process zone is large and undergoing significant damage (plasticity and multiple crack onset sides), and which are likely to trigger plastic deformation of the adherend prior to the self-similar crack growth, this is not the case and in general $\frac{da_{eff}}{d\delta} > \frac{da_{app}}{d\delta}$. However, at least in the case studied, the offset $\left(\frac{da_{eff}}{d\delta} - \frac{da_{app}}{d\delta}\right)$ remains constant throughout the crack propagation stage. Since, from eq. (8), $\frac{da_i}{d\delta} \propto c_1^i$ (where $i = eff$ or app), and, through eq. (6), $c_1^i \propto G_c^{i-\frac{1}{4}}$ the offset must be related to $\left(\frac{da_{eff}}{d\delta} - \frac{da_{app}}{d\delta}\right) \propto \left(G_c^{eff-\frac{1}{4}} - G_c^{app-\frac{1}{4}}\right) = const$. In the case of a non-similar process, $\left(G_c^{eff-\frac{1}{4}} - G_c^{app-\frac{1}{4}}\right) \neq const.$, variation in the offset would be a measure of non-similitude, i.e., the effective parameters would be changing at different rate than the apparent crack growth. As an example, damage at the crack tip without

crack propagation can be considered. In this example, while $\frac{da_{app}}{d\delta} = 0$, the effective crack growth rate $\frac{da_{eff}}{d\delta} \neq 0$ and is changing with the displacement and applied force. Following Fig. 13, this is not observed at least within the crack growth stage, as for both the apparent and the effective parameters follow the derived power laws. Through similitude arguments, the process can be regarded as driven by the elastic strain energy released from the steel adherend.

5.2.4. The R-curve behavior and adherend plasticity

R-curves (G_{I-SBT} and G_{I-CBT}) are summarized in Fig. 14 for both adhesives using eqs. (1) and (2) where $a \equiv a_{app}$. In both cases, the epoxy-based (Fig. 14a) mode I energy release rate is $\leq 15\%$ of the MMA-based (Fig. 14b) counterpart ($G_{I-SBT} = 0.6$ kJ/m^2 vs. 4.0 kJ/m^2 and $G_{I-CBT} = 0.8$ kJ/m^2 vs. 12 kJ/m^2 respectively). However, there are a couple of important remarks that should be highlighted in this context. First of all, the fact that the SBT and CBT are based on the assumption of linear-elastic fracture mechanics (LEFM) of thin bondlines. As the epoxy-based adhesive can be treated more in the framework of LEFM, the difference between the calculated G_{I-SBT} and G_{I-CBT} is not as significant as it is in the case of the MMA-based adhesive. This originates from the fact and the previous observation that $a_{app} \approx a_{eff}$ for the epoxy. For the MMA specimens, the pre-cracking introduced along one of the interfaces led to the asymmetry of the DCB specimen as explained in Section 4.3. Shivakumar et al. [27] concluded that both the CBT and the modified compliance calibration method (MCCT) are valid data reduction techniques to calculate the mode I energy release rate for cracked sandwich beam (CSB) specimens with the delamination/crack artificially created at only one interface between the core and the skin, and in fact they give almost identical results. However, it is expected that the main reason for the difference between the SBT and CBT are related to the fact that $a_{app} < a_{eff}$ for the MMA adhesive. Then, the offset $|\Delta|$ in eq. (2) of the CBT allows to take into account the damage ahead of the apparent crack position and thus improving the accuracy of the estimation. Similar result would be obtained, by inserting a_{eff} directly to eq. (2) and letting $|\Delta| = 0$. Owing to its simplicity, following [21] the CBT method can be recommended as the data reduction approach coping well with the asymmetric DCB configurations and their associated damage zones ahead of the crack tip.

The second remark applies only to the MMA-based case. It was observed experimentally that the steel adherends experienced permanent plastic deformation, and thus one extra energy dissipation mechanism, the steel yielding, should be taken into account in the mode I energy release rate calculations, eqs. (1) and (2). In the present study, in order to investigate the effect of steel yielding on the energy dissipated during the DCB testing, the VCCT model previously discussed in Section
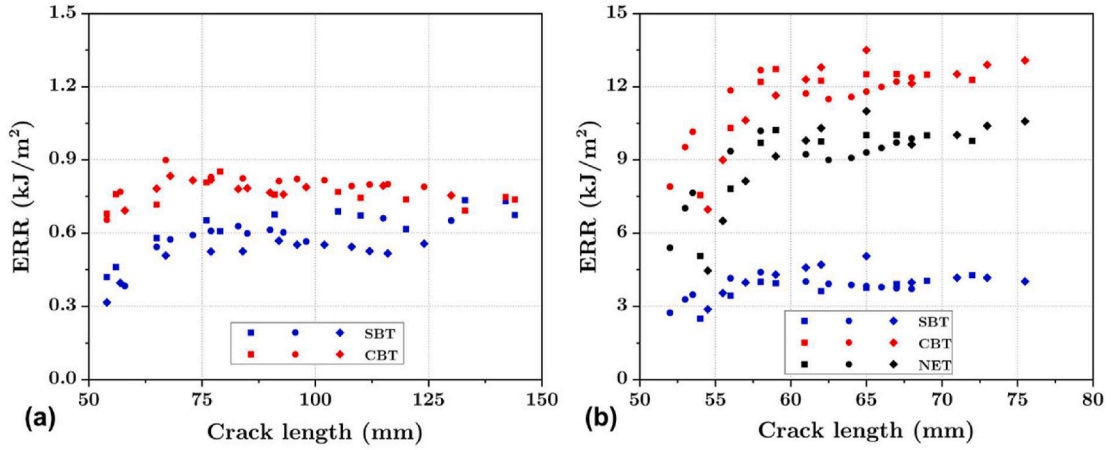
Fig. 14. SBT and CBT DCB mode I strain energy release rate for: (a) epoxy- and (b) MMA-based adhesives on steel adherends.

4.3, was used to simulate two scenarios: one taking into account the adherend plasticity via an elastoplastic model while the other was only linear elastic. Detailed material properties and the in-house adherend elastoplastic response is previously reported in Ref. [12]. According to the simulation results, the steel yielding occurred before the crack started propagating, consistently with the previous discussion. Thus, the observed damage stage in Figs. 11 and 12 is partially due to steel hardening. It is important to highlight that at the maximum force of $\approx$ 1650N (see Fig. 11), hardening is aborted as the crack growth process began. From that moment onwards, the crack propagation continues with no more plastic deformation occurring in the steel adherend as it is invoked by the perfect agreement with the elastic scaling-laws derived. In other words, the "actual/net" energy release rate of the MMA-based specimens can be obtained by subtracting a constant value, corresponding to the energy dissipate due to steel yielding before the crack onset. This "actual/net" energy release rate is hereby represented by G_{I-NET} (see Fig. 14b), and $G_{I-NET} = G_{I-CBT} - \frac{d}{bda} \int_v U_{pl} dV$. The later term

corresponds to the energy dissipated via steel yielding. This term was estimated from VCCT/FE calculations as the difference between the elastoplastic model and the linear elastic model and is approximately 2.5 kJ/m^2. This hypothesis is validated in the upcoming subsection by comparing the analytical predictions against the experimental load-displacement curves of the MMA-based DCB specimens using the calculated ERR in Fig. 14.

5.2.5. Correlation between macroscopic data and direct observations

Fig. 15 shows representative load displacement curves against the

analytical predictions for the epoxy-base and MMA-based specimens. For the initiation linear segment of the load-displacement curve, the SBT [eq. (3)] with $a \equiv a_{app.}$ was used to predict analytically the macroscopic response. For the propagation response, the power-law from eq. (4) was used with a constant average value for the propagation G_I based on the experimental data reported previously in Fig. 14 ($G_{I-SBT} = 0.6$ kJ/m^2 and $G_{I-CBT} = 0.8$ kJ/m^2 for the epoxy and $G_{I-SBT} = 4.0$ kJ/m^2, $G_{I-CBT} = 12.0$ kJ/m^2 and $G_{I-NET} \sim 9.5$ kJ/m^2 for the MMA).

For the epoxy-based predictions in Fig. 15a, there is a good agreement between the SBT, CBT and the experimental results. Moreover, two propagation curves are plotted depicting the average G_{I-SBT} and G_{I-CBT} in blue and red dashed lines respectively. It is clear from the comparison that, once $a \equiv a_{app}$ the SBT underestimates the macroscopic response of the crack propagation while the CBT succeeds in capturing it with an acceptable level of accuracy. This confirms the recommendation by Shivakumar et al. [27] of using the CBT approach for asymmetric DCB specimens.

Moving on to Fig. 15b of the MMA adhesive, significant differences can be observed in both: the initial linear segment and the propagation stage. It becomes evident that SBT (eq. (3)) where $a \equiv a_{app}$ underestimated the initial linear compliance of DCB specimen. This is due to the fact that when taking $a \equiv a_{app}$, SBT does not take into account the effect of the process zone ahead of the crack tip and its length which is significant in the MMA case ($\sim$50 mm). It is interesting to compare these predictions with the fitted linear power-laws in Fig. 11a. While for the epoxy-based, both predictions are similar since in this case $a_{app} \approx a_{eff}$, for the MMA-case the fitted linear power-law is more compliant than the SBT in Fig. 15b, since for MMA-based $a_{app} < a_{eff}$. If one would use in eq
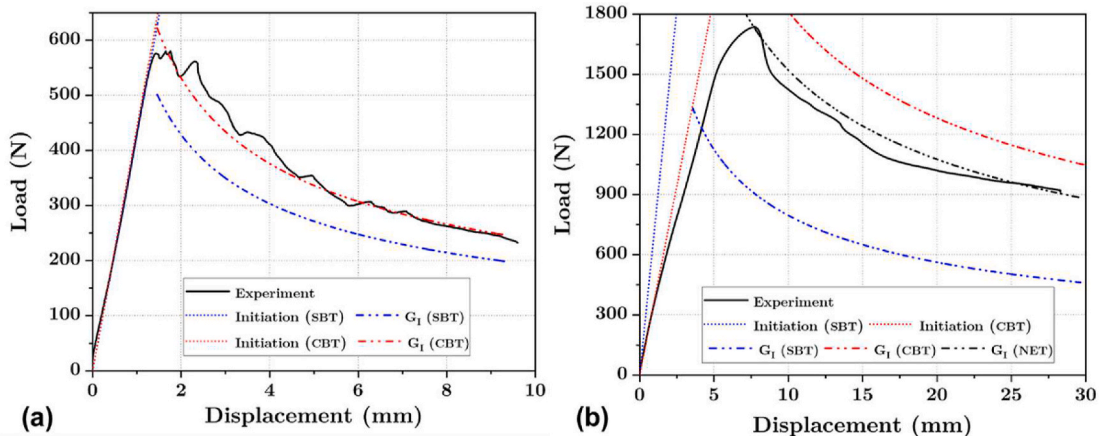

Fig. 15. Representative load–displacement curves (experiment vs. predictions) for the (a) epoxy-based and (b) MMA-based DCB specimens.

(3) $a \equiv a_{eff}$, one would obtain the predicted linear power law shown in Fig. 11a. In terms of the propagation phase, three curves are plotted using the average G_{I-SBT} and G_{I-CBT} and G_{I-NET}. It is very clear that the SBT underestimates the response while the CBT without considering the steel yielding, overestimates it. However, the G_{I-NET} captures well the experimental macroscopic response suggesting that the hypothesis previously put forward, in Section 4.1.4, that the steel yielding effect happens only before the crack propagation is valid.

6. Conclusions

In this work the influence of the adhesive and adherend ductility on the fracture properties and behavior of joints with thick bondlines was investigated. Two types of adhesives were studied: epoxy-based adhesive with representative elastic-brittle behavior, and MMA-based adhesive with elastic-plastic behavior. Both adhesives were characterized in their bulk form as well as bonded steel-to-steel joint under mode I loading. Based on the results obtained the following conclusions can be made:

- The difference in the nature of the two adhesives from a macroscopic point of view is demonstrated via testing the bulk adhesive in tensile (dog-bone) and fracture toughness (CT) loading conditions. In both cases the elastic and relatively brittle nature of the epoxy-based adhesive was obvious when compared against the non-linear and relatively ductile/flexible nature of the MMA-based counterpart.
- When confined, as in the DCB specimen, the MMA bondlines demonstrated various energy dissipation mechanisms in the form of high deformation, multiple cracking, and Poisson's effects as opposed to the relatively brittle epoxy bondlines which fractured with one single crack parallel to the adherends edge at the middle of the adhesive thickness. This resulted in approximately one order of magnitude higher fracture toughness for the MMA bonded specimens as opposed to their epoxy counterparts.
- The existing data reduction techniques for DCB analysis, which are based on LEFM, seems to fall short when it comes to applying them to thick bondlines, adherend plasticity and relatively ductile adhesives. However, they can be tailored and slightly modified to take into account such variations with a reasonable level of accuracy in the predictions, for example, by using $a \equiv a_{eff}$ in the compliance predictions to take into account the length of the fracture process zone and by subtracting the plasticity of the adherends to determine the G_{Ic} of the adhesive.
- In spite of the steel adherend experiencing initial plasticity in the MMA-based adhesively-bonded specimens, the crack growth and fracture parameters could be deduced from the elastic energy release rate.
- DIC was proven to be a successful complementary NDT technique throughout the whole testing campaign capturing the surface strain deformations, crack growth propagation and the FPZ ahead of the crack tip. However, the limitation of such surface measurement technique was also highlighted in the case of the MMA-based adhesive DCB crack growth which did not span the entire width of the specimen. In this case the DIC was only able to capture the edge crack without providing much information about the crack propagation across the specimen's width.
- This study highlights the fact that the use of ductile adhesive instead of the commonly used brittle ones can significantly improve the adhesively bonded joints in real-life application such as maritime applications in which thick bondlines, manufacturing-tolerant and fracture-resistance characteristics are required. This is shown through the CT and DCB fracture mode I testing. In both cases, it was clearly shown that the energy required for crack growth in the MMA "ductile" adhesive as opposed to the epoxy "relatively brittle" counterpart is ~4 and 10 times respectively.

References

[1] Hashim SA. Adhesive bonding of thick steel adherends for marine structures. Mar Struct 1999;12:405–23. https://doi.org/10.1016/S0951-8339(99)00029-5.

[2] Mieloszyk M, Majewska K, Ostachowicz W. Application of embedded fibre Bragg grating sensors for structural health monitoring of complex composite structures for marine applications. Mar Struct 2021;76:102903. https://doi.org/10.1016/j.marstruc.2020.102903.

[3] Kharghani N, Guedes Soares C. Mechanical properties evaluation of the components of a failed hybrid steel-FRP balcony overhang in ships. Mar Struct 2019;68:102647. https://doi.org/10.1016/j.marstruc.2019.102647.

[4] Enabling Qualification of Hybrid Structures for Lightweight and Safe Maritime Transport .. https://www.qualify-euproject.com/(accessed September 30, 2021).

[5] Saeedifar M, Saleh MN, Nijhuis P, de Freitas ST, Zarouchas D. Damage assessment of a titanium skin adhesively bonded to carbon fiber–reinforced plastic omega stringers using acoustic emission. Struct Health Monit 2021. https://doi.org/10.1177/14759217211001752. 147592172110017.

[6] Freitas ST De, Sinke J. Failure analysis of adhesively-bonded metal-skin-to-composite-stiffener : effect of temperature and cyclic loading. Compos Struct 2017; 166:27–37. https://doi.org/10.1016/j.compstruct.2017.01.027.

[7] Heshmati M, Haghani R, Al-Emrani M. Durability of bonded FRP-to-steel jointsEffects of moisture, de-icing salt solution, temperature and FRP type. Compos B Eng 2017;119:153–67. https://doi.org/10.1016/j.compositesb.2017.03.049.

[8] Arouche MM, Saleh MN, Teixeira de Freitas S, de Barros S. Effect of salt spray ageing on the fracture of composite-to-metal bonded joints. Int J Adhesion Adhes 2021;108:102885. https://doi.org/10.1016/j.ijadhadh.2021.102885.

[9] Budzik MK, Wolfahrt M, Reis P, Kozłowski M, Sena- J, Papadakis L, et al. Testing mechanical performance of adhesively bonded composite joints in engineering applications : an overview. J Adhes 2021:1–77. https://doi.org/10.1080/00218464.2021.1953479.

[10] Lopes Fernandes R, Teixeira de Freitas S, Budzik MK, Poulis JA, Benedictus R. From thin to extra-thick adhesive layer thicknesses: fracture of bonded joints under mode I loading conditions. Eng Fract Mech 2019;218:106607. https://doi.org/10.1016/j.engfracmech.2019.106607.

[11] Saleh MN, Saeedifar M, Zarouchas D, De Freitas ST. Stress analysis of double-lap bi-material joints bonded with thick adhesive. Int J Adhesion Adhes 2019:102480. https://doi.org/10.1016/J.IJADHADH.2019.102480.

[12] Saeedifar M, Saleh MN, De Freitas ST, Zarouchas D. Damage characterization of adhesively-bonded Bi-material joints using acoustic emission. Compos B Eng 2019; 176. https://doi.org/10.1016/j.compositesb.2019.107356.

[13] Lopes Fernandes R, Budzik MK, Benedictus R, Teixeira de Freitas S. Multi-material adhesive joints with thick bond-lines: crack onset and crack deflection. Compos Struct 2021;266. https://doi.org/10.1016/j.compstruct.2021.113687.

[14] Marzi S, Biel A, Stigh U. On experimental methods to investigate the effect of layer thickness on the fracture behavior of adhesively bonded joints. Int J Adhesion Adhes 2011;31:840–50. https://doi.org/10.1016/j.ijadhadh.2011.08.004.

[15] Carlberger T, Stigh U. Influence of layer thickness on cohesive properties of an epoxy-based adhesive-an experimental study. J Adhes 2010;86:816–35. https://doi.org/10.1080/00218464.2010.498718.

[16] Daghayni HR, Ye L, Mai Y-W. Mixed-mode fracture of adhesively bonded CF/epoxy composite joints. J Compos Mater 1996;30:1248–65.

[17] Martin J. Methyl methacrylate (MMA) adhesives – a trending procedure in the marine industry. Reinforc Plast 2020;64:204–7. https://doi.org/10.1016/j.repl.2019.10.006.

[18] Jaiswal PR, Kumar RI, Saeedifar M, Saleh MN, Luyckx G, Waele W De. Deformation and damage evolution of a full-scale adhesive joint between a steel bracket and a sandwich panel for naval application. Proc Inst Mech Eng Part C 2020;235(3). https://doi.org/10.1177/0954406220947122.

[19] ISO 8501-1:2007 Preparation of steel. Substrates before application of paints and related products — visual assessment of surface cleanliness — Part 1: rust grades and preparation grades of uncoated steel substrates and of steel substrates after overall re. 2007. https://doi.org/10.31030/9871577.

[20] ISO 25217: Adhesives. Determination of the mode 1 adhesive fracture energy of structural adhesive joints using double cantilever beam and tapered double cantilever beam specimens 2009. 2006. p. 13.

[21] Heide-Jørgensen S, Budzik MK. Effects of bondline discontinuity during growth of interface cracks including stability and kinetic considerations. J Mech Phys Solid 2018;117:1–21. https://doi.org/10.1016/j.jmps.2018.04.002.

[22] Ben Salem N, Budzik MK, Jumel J, Shanahan MER, Lavelle F. Investigation of the crack front process zone in the double cantilever beam test with backface strain monitoring technique. Eng Fract Mech 2013;98:272–83. https://doi.org/10.1016/j.engfracmech.2012.09.028.

[23] Savioli RG, Ruggieri C. J and CTOD estimation formulas for C(T) fracture specimens including effects of weld strength overmatch. Int J Fract 2013;179: 109–27. https://doi.org/10.1007/s10704-012-9781-4.

[24] ASTM E1820. Standard test method for measurement of fracture toughness, vols. 1–54. ASTM B Stand; 2013. https://doi.org/10.1520/E1820-13. Copyright.

[25] Fleck NA, Hutchinson JW, Zhigang S. Crack path selection in a brittle adhesive layer. Int J Solid Struct 1991;27:1683–703. https://doi.org/10.1016/0020-7683(91)90069-R.

[26] Tao R, Li X, Yudhanto A, Alfano M, Lubineau G. On controlling interfacial heterogeneity to trigger bridging in secondary bonded composite joints: an efficient strategy to introduce crack-arrest features. Compos Sci Technol 2020;188: 107964. https://doi.org/10.1016/j.compscitech.2019.107964.

[27] Shivakumar K, Chen H, Smith SA. An evaluation of data reduction methods for opening mode fracture toughness of sandwich panels. J Sandw Struct Mater 2005; 7:77–90. https://doi.org/10.1177/1099636205047085.